TU Delft

Delft University of Technology

The fundamental operation mechanisms of nc-$SiO_{X\geq0}$:H based tunnel recombination junctions revealed

de Vrijer, Thierry; van Nijen, David; Parasramka, Harsh; Procel Moya, Paul A.; Zhao, Yifeng; Isabella, Olindo; Smets, Arno H.M.

DOI
10.1016/j.solmat.2021.111501

Publication date
2022

Document Version
Final published version

Published in
Solar Energy Materials and Solar Cells

Citation (APA)
de Vrijer, T., van Nijen, D., Parasramka, H., Procel Moya, P. A., Zhao, Y., Isabella, O., & Smets, A. H. M. (2022). The fundamental operation mechanisms of nc-$SiO_{X\geq0}$:H based tunnel recombination junctions revealed. *Solar Energy Materials and Solar Cells*, *236*, Article 111501. https://doi.org/10.1016/j.solmat.2021.111501

Important note
To cite this publication, please use the final published version (if applicable).
Please check the document version above.

Copyright
Other than for strictly personal use, it is not permitted to download, forward or distribute the text or part of it, without the consent of the author(s) and/or copyright holder(s), unless the work is under an open content license such as Creative Commons.

Takedown policy
Please contact us and provide details if you believe this document breaches copyrights.
We will remove access to the work immediately and investigate your claim.

This work is downloaded from Delft University of Technology.
For technical reasons the number of authors shown on this cover page is limited to a maximum of 10.

Solar Energy Materials & Solar Cells 236 (2022) 111501

Contents lists available at ScienceDirect

Solar Energy Materials and Solar Cells

journal homepage: www.elsevier.com/locate/solmat

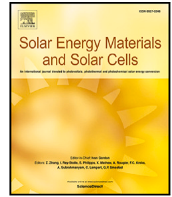

The fundamental operation mechanisms of nc-SiO$_{X\geq0}$:H based tunnel recombination junctions revealed

Thierry de Vrijer [a,*], David van Nijen [a], Harsh Parasramka [a], Paul A. Procel Moya [a,b], Yifeng Zhao [a], Olindo Isabella [a], Arno H.M. Smets [a]

[a] Photovoltaic Materials and Devices, TU Delft, Mekelweg 4, Delft 2628CD, The Netherlands
[b] Instituto de Micro y Nanoelectrónica, Universidad San Francisco de Quito, Diego de Robles s/n, Quito 170901, Ecuador

ARTICLE INFO

Keywords:
Tunnel recombination junction
Multijunction
Tandem PV
Silicon heterojunction
Thin film silicon
Amorphous silicon
Nano-crystalline silicon
Amorphous silicon germanium

ABSTRACT

Two terminal multi-junction (MJ) photovoltaic (PV) devices are well established concepts to increase the solar-to-electrical power conversion in reference to single PV junctions. In multi-junction PV devices two consecutive sub-cells are interconnected using a tunnel recombination junction (TRJ) in which the light excited holes of one sub-cell recombine with the light excited electrons of the other sub cell. An ideal TRJ is an ohmic contact with non-rectifying behaviour. TRJ's based on p- and n-doped silicon-oxides have been successfully applied in a variety of hybrid multi-junction PV devices in which tunnelling and trap-assisted tunnelling over width of 5–20 nm rules the TRJ's recombination kinetics.

In this contribution the qualitative fundamental working principles of tunnel recombination junctions based on p- and n-doped silicon and silicon-oxide alloys are revealed using both electrical modelling and experiments based on a unique set of tandem lab cells (four types based on four different PV materials) combined with structural variations in TRJ architectures. The study results in design rules for the integration of silicon-oxide based TRJ's and provides fundamental insights into the sensitivity of the electrical performance of the TRJ's to doping concentrations, to alignment of the conduction and valence bands of consecutive sub-cells, to the nature of interface defects, to the growth of amorphous and crystalline phases and its dependence on substrate or seed layers and to the nanoscale thicknesses of the TRJ layers.

1. Introduction

Multijunction photovoltaic (PV) devices are a logical next step for further reducing the cost price per Watt peak of PV, by increasing the yield per area. In particular, tandem PV devices with a crystalline silicon (c-Si) bottom cell are receiving increased attention. These c-Si bottom cells are combined with a range of PV technologies, such as perovskites [1–3], C(I)GS [4], III-V technologies such as GaInP/GaAs [5] and GaAsP [6] or nano-c-Si top cells [7,8]. In multijunction devices charge carriers are photo-generated in each individual subcell. In two-terminal multijunction devices, in case of a p-type front contact, electrons generated in the top junction and holes generated in the bottom junction need to recombine at the interface between the two subcells, at the so-called tunnel recombination junction (TRJ). An ideal TRJ, one that facilitates this recombination between subcells, is an Ohmic contact with non-rectifying behaviour. When not properly engineered, the TRJ can act as a p–n junction with a reverse direction to that of the subcells.

In multijunction devices with a silicon-based bottom cell generally nanocrystalline silicon (nc-Si:H) or nanocrystalline silicon-oxide (nc-SiO$_X$:H) based TRJ's are used [9–15]. The performance of PV cells is very sensitive to the p-doped layer in particular, as achieving desirable doped layer properties such as low activation energy, high conductivity and optical transparency is inherently more challenging in p-doped layers in reference to n-doped layers [16,17]. Moreover, interpreting the fundamental effect of changes to individual doped layers in the TRJ, based on device performance, is challenging. The p-doped (p-) layer determines the energetic alignment in, and thereby performance of, the subcell it is a part of. It also determines the electrical characteristics, and consequently the effectiveness, of the TRJ. Additionally, from a processing perspective, the p-layer can affect the subsequent growth of the n-layer just as the p-layer growth can be influenced by the preceding layer. To distinguish between these effects and functionalities, the investigated nc-Si(O$_X$):H based TRJ's should be integrated in different device architectures and multijunction configurations, including absorber layers with different crystalline phase fractions, band gap

* Corresponding author.
E-mail address: t.devrijer@tudelft.nl (T. de Vrijer).

https://doi.org/10.1016/j.solmat.2021.111501
Received 3 August 2021; Received in revised form 8 November 2021; Accepted 9 November 2021
Available online 8 December 2021
0927-0248/© 2021 The Authors. Published by Elsevier B.V. This is an open access article under the CC BY license (http://creativecommons.org/licenses/by/4.0/).

Table 1
Conditions used for the various PECVD processed layers. i-nc-Si:H processed at 40 MHz, all other layers at 13.56 MHz.

	P_{RF}	p	T_S	F_{SiH4}	F_{GeH4}	F_{H2}	F_{CO2}	F_{PH3} (2%)
	(mW–cm^{-2})	(mbar)	(°C)	(sccm)	(sccm)	(sccm)	(sccm)	(sccm)
i-a-SiGe:H	27.8	3.6	180	30	0.4–5.3	200	–	–
i-a-Si:H (absorber)	62.5	10	120	2	–	200	–	–
i-a-Si:H (SHJ)	27.8	0.6	180	40	–	–	–	–
i-nc-Si:H	278	4	180	1.2/3.5	–	120	–	–
n-nc-SiO$_X$:H	76.4	1.5	180	1	–	120	1.6	2
n-nc-Si:H	76.4	1.5	180	1	–	120	–	3
n-a-Si:H	27.8	0.6	180	40	–	–	–	11

energies and stoichiometries. This allows for the isolation of the impact of the TRJ, from the opto-electrical nature of the subcells, on the device performance.

To achieve this isolation, and considering the sensitivity of device performance to the p-layer properties in particular, in this work, the effect of changes to the p-layer are investigated across four different multijunction PV device architectures. These are tandem devices consisting of a wafer-based silicon heterojunction (SHJ) subcell and subcells with hydrogenated nanocrystalline silicon absorbers, hydrogenated amorphous silicon germanium (a-SiGe:H) absorbers and hydrogenated amorphous silicon (a-Si:H) absorbers, in various configurations. The plasma enhanced chemical vapour deposition (PECVD) processed devices are schematically shown in Fig. 1. TRJ operation is investigated by varying the deposition conditions, thickness and design of the p-layer of the bottom junction. Moreover, electrical simulations are performed to qualitatively support findings from the experimental results, in order to reveal the fundamental operation mechanisms that determine the performance of tunnel recombination junctions.

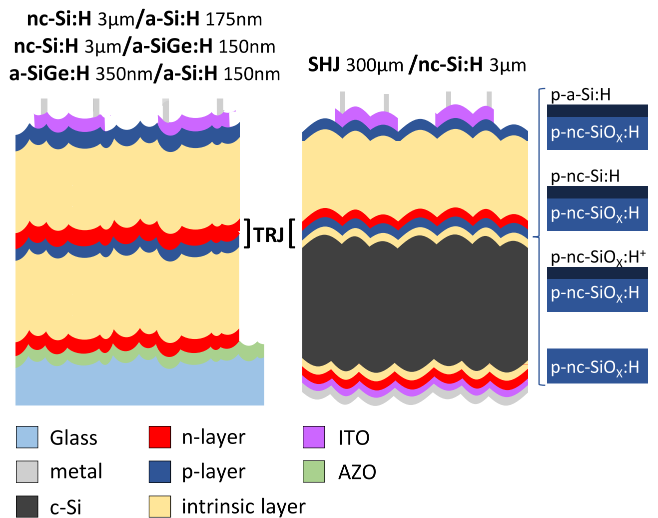

Fig. 1. Schematical representation of the four different device architectures presented in this work. All devices are processed in n-i-p/n-i-p substrate configuration. Absorber layer thicknesses for thin film nc-Si:H/a-Si:H, nc-Si:H/a-SiGe:H and a-SiGe:H/a-Si:H devices (left) and SHJ/nc-Si:H (right) tandem devices are indicated above the structure. Small blue visuals on the right indicate the four different p-layer stacks used in this work.

2. Experimental section

2.1. Processing tandem devices

In this work the results of four different tandem device architectures are presented. These are tandem devices consisting of a SHJ subcell and a subcell with a nc-Si:H absorber, a nc-Si:H subcell combined with either an a-SiGe:H absorber or a-Si:H absorber and finally a tandem device consisting of an a-SiGe:H subcell and an a-Si:H subcell. The devices are processed using a radiofrequency PECVD cluster tool. The variations within experimental series are exclusively applied to the p-layer in the TRJ. As the 100+ tandem PV devices developed for this work are processed over a period of 2 years on a lab-scale PECVD tool, some variations to supporting layers exist between experimental series. These variations include absorber thickness variations, affecting which of the subcells is current limiting. Such variations do not exist within an experimental series, where "experimental series" in this work is defined as a set of devices processed at a given point in time, for which no variations exist in architecture and processing conditions other than the intended variations to the p-layer in the TRJ.

Precursor gas flow rates are indicated by (F_{gas}). Diborane (B_2H_6) is used as a precursor gas for boron doping. The reported diborane gas flow rates are 0.02% B_2H_6 in H_2. The reported phosphine (PH_3) flow rates, used as the precursor for phosphorus doping, are 2% PH_3 in H_2. Silane (SiH_4) and carbon-dioxide (CO_2) are used as silicon and oxygen precursors, respectively. The n-doped (n-) layer of the top junction, the n-layer that is part of the TRJ, consists of an n-nc-Si:H 5nm/nc-SiO$_X$:H 15nm/n-a-Si:H 5 nm stack starting from the p-layer of the bottom junction. The deposition conditions of the absorber materials and doped layers are indicated in Table 1. A schematic representation of the tandem devices is shown in Fig. 1.

The three tandem devices that combine two thin film junctions (nc-Si:H, a-SiGe:H, a-Si:H) are processed in n-i-p/n-i-p substrate configuration on textured Corning Eagle XG glass. The texturing process was developed by [18,19] and is explained in more detail elsewhere [20]. A 700 nm aluminium-doped zinc oxide (AZO) layer is sputtered onto the textured glass for use as a transparent back contact. No back reflector is used, as the situation with minimal back reflection provides the most straightforward comparison of variations in the TRJ and the generated J_{SC}, V_{OC} and FF. The front contact consists of a transparent conductive oxide (TCO), a sputtered 75 nm indium-doped tin oxide (ITO) layer, in combination with a 500 nm aluminium front grid, which is deposited through thermal evaporation. The i-nc-Si:H absorber layer has a thickness of about 3 μm, the i-a-Si:H absorber layer has a thickness of about 175 nm. The i-a-SiGe:H absorber layers have a profiled bandgap energy across the absorber width. Bandgap profiling is achieved by varying the relative GeH_4 flow rate during deposition. The used absorber profile is different for the nc-Si:H/a-SiGe:H and a-SiGe:H/a-Si:H tandem devices. When used as the top junction in the tandem device (nc-Si:H/a-SiGe:H) a maximum GeH_4 flow rate of 3.3 sccm with a plateau fraction of 0% (a V-shaped absorber profile), i/p-region width of 20 nm and absorber thickness of 175 nm is used. When used as the bottom junction (a-SiGe:H/a-Si:H) a maximum GeH_4 flow rate of 5.3 sccm is used, with a plateau fraction of 30% (U-shaped profile), i/p-region width of 20 nm and absorbed thickness of 350 nm. More information about the used bandgap profiles can be found in [20].

For the SHJ processing, Topsil Floatzone n-type ⟨100⟩ mono-crystalline silicon wafers are used with a thickness of 300 μm. These wafers are then textured using a two-step approach. First a 10 min Tetramethylammoniumhydroxide etch and rinse was applied, followed by an acidic poly-etch, consisting of 1 part HF (40.5% wt. in H_2O), 6 parts HNO_3 (69.5% wt. in H_2O) and 3 parts H_2O. This results in smooth pyramidal surface features on both sides of the wafer. More information about the development, optical behaviour and surface passivation of

this texturing approach can be found elsewhere [21]. The backside of the wafer is finished by subsequently processing 10 nm i-a-Si:H layer and 10 nm n-a-Si:H layer. This is followed by a full area 150 nm sputtered ITO layer and an evaporated metal contact consisting of 300 nm Ag/30 nm Cr/800 nm Al. On the front side of the wafer an i-a-Si:H layer is processed followed by a p-layer and the n-i-p junction with i-nc-Si:H absorber. The front contact, 75 nm ITO and 500 nm Al, is similar to the other tandem devices.

2.2. Measuring tandem devices

The external quantum efficiency (EQE) was measured using an in-house EQE setup at TU Delft, consisting of a Xenon lamp and a monochromator for spectral data acquisition. To measure both junctions separately, bias light was used to saturate the top and bottom cell in turn. The top cell was saturated using light with wavelengths between 365 nm and 530 nm, while the bottom cell was saturated with light between 800 nm and 950 nm. The J–V measurements of the solar cells were conducted using an AM1.5$_G$ solar simulator at an illumination of 100 mW cm^{-2} under a controlled temperature of 25 °C. The open-circuit voltage (V_{oc}) and fill factor (FF) were extracted from the J-V curves. Each tandem device consists of a single substrate, on which 24 individual cells with an area of 16 mm^2 were processed. All 24 cells on the substrate were measured. The results presented in this work are the average of the 5 best performing cells on each substrate. For each of the four different tandem configurations, the J-V curves and external device characteristics of the cell with the highest conversion efficiency and the highest $V_{oc}*FF$ product can be found in the supplementary information.

2.3. Electrical simulations

In this work energy band diagrams are presented of a range of TRJ's to qualitatively and visually support interpretation of the observed trends. The simulations were performed using TCAD Sentaurus [22]. For the simulations uniform materials were assumed with experimentally obtained bandgap and activation energies. To evaluate the energy alignment, Poisson equations were solved, assuming equipotential electrodes. The models and material related parameters used to simulate the device structures presented in this work are reported in [23]. The energy band diagrams are shown under equilibrium conditions, in the dark. The energy alignment is at the core of charge transport. Accordingly, band diagrams under equilibrium illustrate concisely and simply the fundamental mechanisms for charge transport. Adding operational conditions, such as light injection and an applied potential to the band diagrams add more complexity and would make the obtained diagrams less suited for the purpose of qualitatively supporting interpretation of experimentally observed trends.

3. Results and discussion

3.1. Loss mechanisms in tandem devices

There are several ways in which the properties of the p-doped layer in a TRJ can result in losses to the V_{oc} and FF in a tandem device. Most straightforward, the material properties of the p-layer determine the performance of the bottom n(-i)-p junction. Fundamentally speaking, the active acceptor dopant concentration (N_A) can increase the built-in voltage (V_{bi}) across the i-layer in the bottom cell, since

$$V_{bi} \sim \ln\left(\frac{N_A}{n_i}\right) \quad (1)$$

where n_i is the intrinsic carrier concentration. The active dopant concentration, amongst other material properties such as the stoichiometry [20], material phase fractions in heterogeneous materials and the material density [16], can also influence the bandgap energy E_G and activation energy E_{act} of the p-layer. This in turn influences the energetic band alignment at the i/p-interface of the bottom cell, which can significantly affect the V_{bi} in a drift device, according to [24]:

$$qV_{bi} = E_G - E_{Fn} - E_{Fp} \quad (2)$$

where E_G is the band gap energy of the intrinsic absorber layer and E_{Fn} and E_{Fp} are the Fermi energy levels in the n- and p-doped layer, respectively. With no significant variations in the work function of the p-layer, which we can assume according to [25], and with the i-layer and n-layer deposition conditions remaining constant, changes in E_G or E_{act} of the p-layer will have an effect on E_{Fp} and consequently on the built-in voltage in the device. The p-layer material properties do not only affect the device voltage directly. A variation in the optical transparency or refractive index of the p-layer in the TRJ can influence the transmission into the bottom cell. This results in changes in the generated photo-current density (J_{ph}), which influences the V_{oc} according to:

$$V_{oc} \sim \ln\left(\frac{J_{ph}}{J_0}\right) \quad (3)$$

While this effect is generally minor, variations in the recombination current density (J_0) are not. The J_0 is an indicator of the charge carrier recombination in a device, and the i/p-interface is well known for being a significant recombination site in thin film silicon devices, if not well-engineered [26–28].

All these effects influence the performance of the bottom cell in the device. If we consider the p-layer as part of TRJ in a multijunction device, additional complexity is added. As mentioned, in n-(i-)p/n-i-p tandem PV devices, the TRJ should facilitate the recombination of holes from the bottom cell with electrons from the top cell to prevent non-ohmic behaviour. As the FF is a measure of the resistive losses in a photovoltaic device, it will be affected by a p-layer that results in a poorly engineered TRJ or i/p-interface. Additionally, in tandem devices the FF is subject to the mismatch between the current density generated in the top and bottom cell [29,30]. Variations in the refractive index or optical transparency of the p-layer can affect the current matching between both junctions [9,13,15], consequently affecting the FF. Moreover, the FF can vary depending on which of the subcells is current limiting. These combined effects can make pinpointing the origin of observed trends in tandem devices challenging. The latter two challenges are mitigated in this work, to a certain extent, by performing experiments across different device architectures with different current matching conditions and current limiting subcells.

3.2. Influence of p-nc-SiO$_X$:H deposition conditions on the performance of tandem a-Si:H/nc-Si:H solar cells

The influence of variations in the F_{B2H6} during deposition of the p-layer of the bottom junction in nc-Si:H/a-Si:H tandem devices are reported in Fig. 2. A trade-off can be observed between the V_{oc} and FF as a function of F_{B2H6}. Increasing F_{B2H6} from 10 to 15 sccm, for instance, increases the FF from 56% to 61.8%, while the V_{oc} is decreased by 54 mV.

The opto-electrical properties of p-nc-SiO$_X$:H are a function of the relative a-SiO$_X$:H, nc-Si:H and a-Si:H material phase fractions, the density of the amorphous phase and the active dopant concentration [16]. An increase of F_{B2H6} can result in the suppression of crystalline growth, a decrease in a-SiO$_X$:H phase fraction and potentially in an increase of the active doping concentration [16]. It is difficult to determine which of these effects results in the observed V_{oc} and FF trends. A decrease of the a-SiO$_X$:H phase fraction results in a decrease of the bandgap energy near the i/p-interface, which can result in the observed V_{oc} decrease, according to Eq. (2). At the same time, an increase of F_{B2H6} can results in an increase of the active dopant concentration, increasing V_{oc} according to Eq. (1). A competition between these two effects could result in the observed V_{oc} trends as a function of F_{B2H6}.

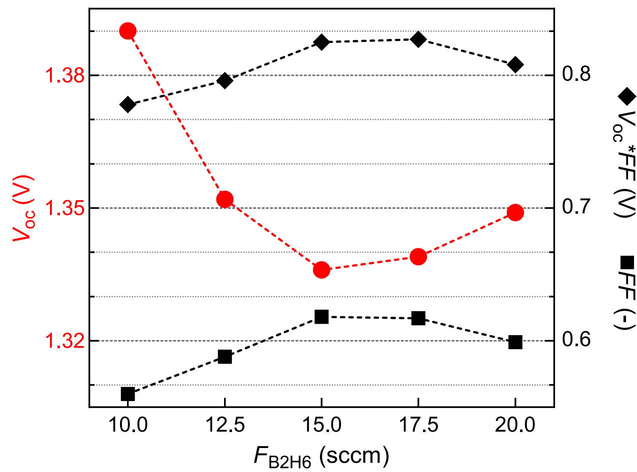

Fig. 2. The V_{oc} (red circles, left y-axis), FF (black squares, right axis) and $V_{oc}*FF$ product (black diamonds, right axis) of nc-Si:H/a-Si:H tandem solar cells as a function of the diborane gas flow rate of the p-nc-SiO_X:H layer in the tunnel recombination junction. The p-layer stack consists of a single p-nc-SiO_X:H layer. All samples are processed at F_{H2}=170 sccm and F_{CO2}=1.8 sccm.

The FF also exhibits an optimum in the investigated range. Crystalline tissue in p-nc-SiO_X:H grows in filaments [31–33]. These filaments are essential for transverse carrier transport through the p-layer. With increasing F_{B2H6} crystalline growth will be suppressed [16,34,35]. As a result, carrier transport might suffer, leading to additional resistive losses and a FF decrease. Additionally, sufficient amorphous tissue is required to passivate the crystalline grains and crystalline phase at the i/p-interface [28]. An increase of the amorphous phase faction could improve this passivation, improving the FF. This trade-off might result in the observed optimum of the FF. Alternatively, as deposition time was kept constant, an increase of F_{B2H6} can result in an increase of the deposition rate [16,36,37], and consequently in thicker p-nc-SiO_X:H layers. This can impact the V_{oc} and FF of the tandem devices, as will be discussed in more detail in the next section.

The results presented in Fig. 2 indicate that variations in F_{B2H6} largely results in trade-offs between V_{oc} and the FF. Four additional series of tandems devices, not presented here, in which the F_{H2} and F_{CO2} were varied for different F_{B2H6} values showed similar trade-offs without significant overall improvements in $V_{oc}*FF$. These combined results indicate that there is a limit to the gains than can be realized by exclusively changing the opto-electrical properties of the p-nc-SiO_X:H, using a single unprofiled p-nc-SiO_X:H layer.

3.3. Influence of p-nc-SiO_X:H thickness on the performance of tandem a-Si:H/nc-Si:H solar cells

Next, we investigate the influence of the thickness of the p-layer in the TRJ of tandem PV devices. The EQE curves in Fig. 3(Top) show a significant increase of both the top and bottom cell, when the thickness of the p-doped layer is increased from 6 nm to 18 nm. Reflection measurements, presented in the supplementary information, show no significant change in the front reflection of the devices, indicating an electrical rather than an optical effect. Both junctions are measured separately, while the opposite junction is saturated with bias light. As such, we can observe the effectiveness of generation and collection in each junction in turn. Both junctions, for thin p-layers, have a similar EQE limit. Moreover, the EQE increases to a similar degree with increasing p-layer thickness. This indicates that for a p-layer thickness below 18 nm, collection in the tandem device is limited by the TRJ. From 18 nm to 22 nm the device no longer seems to be limited by the TRJ, as the EQE of the top cell only shows a minor increase, while the bottom cell EQE is decreased. This latter effect can also be observed in

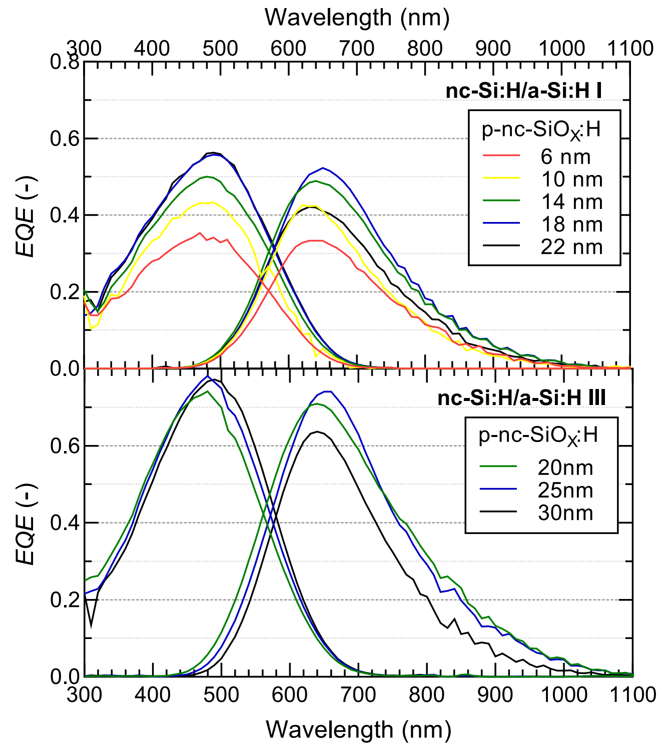

Fig. 3. External Quantum Efficiency plots of the top and bottom junctions of two separate series of nc-Si:H/a-Si:H tandem devices. The thickness of the p-nc-SiO_X:H layer in the tunnel recombination junction of the tandems is varied. Experimental series **I** (top) is processed with a single p-nc-SiO_X:H layer while series **III** (bottom) is processed with a p-nc-SiO_X:H/p-nc-Si:H bi-layer configuration.

Fig. 3(Bottom), where the EQE curves of another series of tandem nc-Si:H/a-Si:H devices are plotted. This is likely an optical effect as more light is reflected back into the top cell and less light transmitted into the bottom cell with increasing p-nc-SiO_X:H thickness, which is in line with earlier reports [9,13,38–40].

In order to analyse these effects, electrical simulations of the TRJ have been performed. A schematic band diagram of the TRJ as a function of the p-nc-SiO_X:H thickness is shown in Fig. 5. The visual shows the energetic band alignment at the i/p-, p/n- and n/i-interfaces, for p-nc-SiO_X:H layers with a thickness of 5 nm, 10 nm, 15 nm and 20 nm and constant activation energy (E_{act}) and bandgap energy E_G. Considering that free electrons reside in the conduction band and move down slope, while holes move up-slope in the valence band, electrons photo-generated in the top junction will have a tendency to accumulate at the p/n-interface, at position **I**. Similarly, holes generated in the bottom junction will have a tendency to accumulate at the i/p-interface, at position **II**. Note that the desired recombination event is one in which an electron from the top junction, from position **I**, recombines with a hole from the bottom junction, at position **II**. This recombination event is most likely to occur through a defect assisted process, referred to as trap-assisted tunnelling in several simulations studies involving tunnelling junctions [25,41]. In order for this tunnelling event to take place, the holes need to overcome an energy barrier, indicated by the coloured areas in the valence band in Fig. 5. As can be understood from this figure, the energy barrier consists of a spatial and energetic component; the best tunnelling junction is one in which the position **I** and **II** are energetically aligned and spatially close. For efficient TRJ operation, apart from effectively directing holes towards p/n-interface, electrons from the bottom junction should be effectively shielded from the p/n-interface, lest they contribute to the accumulation of electrons at position **I** or increase SRH-recombination inside the p-layer. The energy barrier against electron movement to the tunnelling junction is

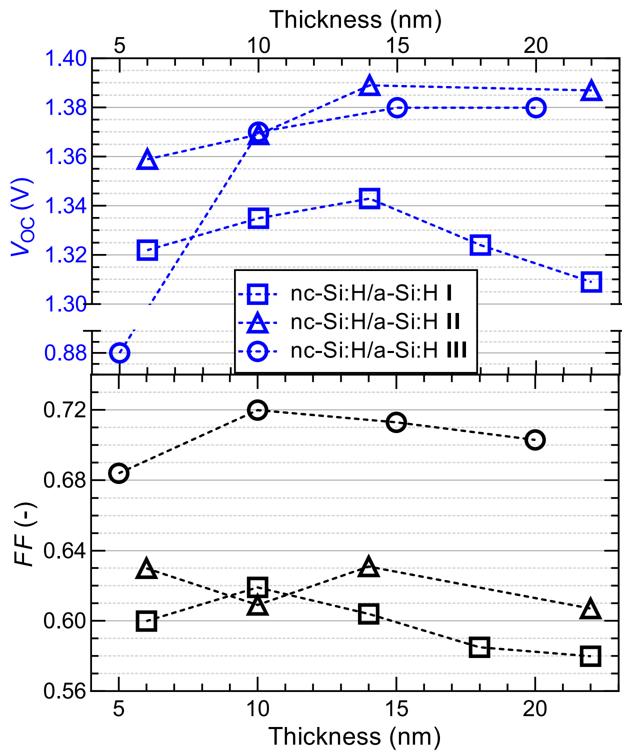

Fig. 4. The V_{oc} (Top) and FF (bottom) of tandem nc-Si:H/a-Si:H devices as a function of p-nc-SiO$_X$:H thickness. The icons represent three separate experimental series, where the **I**(squares) and **II**(triangles) are processed with a single p-nc-SiO$_X$:H layer and series **III**(circles) is processed with a p-nc-SiO$_X$:H/p-nc-Si:H bi-layer configuration.

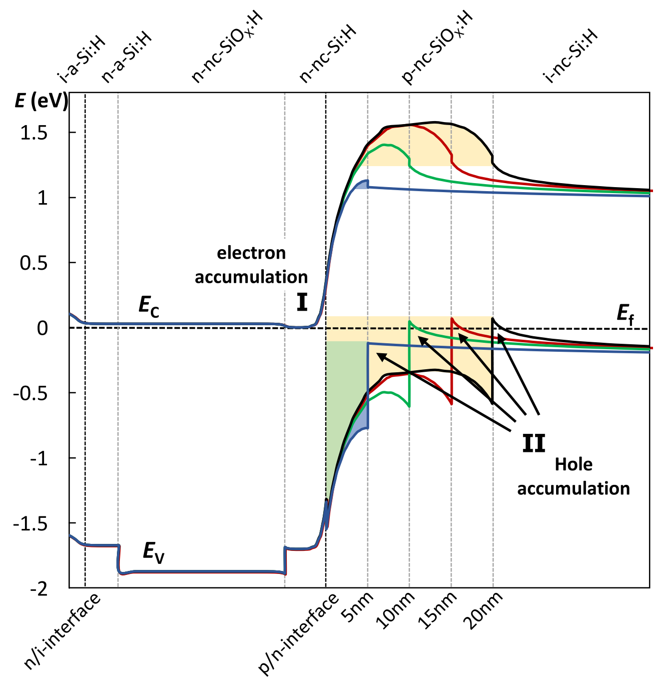

Fig. 5. Electrical simulations of the TRJ under equilibrium conditions in the dark. The energy band diagrams are shown for a p-nc-SiO$_X$:H thickness of 5 nm (blue), 10 nm (green), 15 nm (red) and 20 nm (black). For all thicknesses the conduction band edge E_C and valence band edge E_V are shown. The energy levels of the band edges are indicated in reference to the Fermi energy level E_f, positioned at 0 eV. The materials presented in the plots are indicated on top of the band diagram. The n/i-interface and p/n-interfaces are indicated below the band diagram. Position **I** and **II**, the electron and hole accumulations sites, are referenced in the text. The coloured areas indicate the energy barriers for holes (bottom) and electrons (top), respectively. The blue areas indicated the barrier for a p-nc-SiO$_X$:H layer thickness of 5 nm, while the yellow areas indicates the barriers for a 20 nm p-nc-SiO$_X$:H layer. The green area indicates an overlap between the two barriers.

indicated by the coloured areas in the conduction band in Fig. 5. Both ineffective hole transport and poor electron-shielding can result in the built-up of charge at position **I** and/or **II**, and the creation of a reverse electric field across the TRJ.

The visual provides excellent insight into the nature of the p-thickness related collection issue. It can be observed that at a p-nc-SiO$_X$:H layer thickness of 5 nm (blue curves), there is a large energy barrier against hole movement, indicated by the blue/green area (bottom), and position **I** and **II** are energetically poorly aligned. Moreover, there is hardly an energy barrier, indicated by the blue area (top), against the movement of electrons from the bottom junction to the p-layer and even towards position **I**. When the thickness is increased, band-bending in the p-layer is shifted upwards. As a result, at a p-nc-SiO$_X$:H thickness of 10 nm (green curve), position **I** and **II** are energetically well aligned, the hole barrier is decreased and the energy barrier against electron movement is significantly increased. When the thickness is further increased to 15 nm (red curve), the conduction band edge in the p-layer is further shifted upwards. Consequently, the energy barrier against electron movement is further increased with respect to the energetic barrier against hole movement, improving the TRJ recombination efficiency. Simply put, with the electrical properties of the p-nc-SiO$_X$:H layer being what they are, a minimum p-layer thickness is required for the p-doped layer to fulfil its function in the bottom junction as an electron shield a semi-permeable membrane for holes. It should be noted that the assumption of a constant E_{act} and E_G as a function of thickness is potentially a simplification. The p-layer effectiveness as a function of thickness could additionally be improved as the E_G and E_{act} evolve along the growth direction [16].

The influence of the p-nc-SiO$_X$:H thickness on the V_{oc} and FF of three separate series of tandem nc-Si:H/a-Si:H devices is plotted in Fig. 4, where series **I** and **II** have a single p-nc-SiO$_X$:H layer (and different top junction design) and series **III** has a bi-layer configuration. The bi-layer is schematically visualized in Fig. 1 with a p-nc-SiO$_X$:H layer and a thin 3–5 nm p-nc-Si:H contact layer at the interface with the n-layer. A few things are apparent from these results. 1. the FF is rather sensitive to the p-layer thickness and has optimum in the range of 10–15 nm. 2. An optimal V_{oc} is achieved for p-layer thicknesses in the range 15–20 nm. For series **I** and **III** the V_{oc} decrease for a p-layer thicknesses exceeding 15 nm is minimal within the reported range, which is unlike the trend for the FF. This seems to indicate that for an optimal V_{oc} a minimal rather than a specific optimal p-layer thickness is required, or at least that there is a greater range of optimal thicknesses. In terms of V_{oc}*FF product, optimal performance is realized for a thickness of about 15 nm. These trends in V_{oc} and FF can also be understood from the simulations shown in Fig. 5. As the thickness is increased from 5 nm to 15 nm, the band bending at the i/p-interface changes. As a result, the difference between the Fermi level and the valence band edge at the i/p-interface is decreased, and V_{bi} is increased according to Eq. (2), resulting in the observed increase in V_{oc}. Fig. 5 shows that this is no longer true if the thickness is further increased beyond 15 nm; the V_{oc} improvement reaches an optimum. Further increasing the thickness beyond this point increase the distance a hole has to travel through the p-layer, increasing resistance against this movement, as the defect density in the p-nc-SiO$_X$:H layer is assumed to be much higher than in the i-layer. Consequently, J_0 is increased, decreasing V_{oc} according to Eq. (3). Alternatively, the V_{oc} increase of the tandem devices, with p-nc-SiO$_X$:H thickness, can be understood to be the result of a decrease of the reverse electric field across the TRJ. A similar effect results in the observed trend for the FF, although that is better explained in terms of resistances. From 5 nm to 10–15 nm, as a result of improved electron shielding, the shunt resistance is increased as the free movement from electrons from the bottom to the top junction is

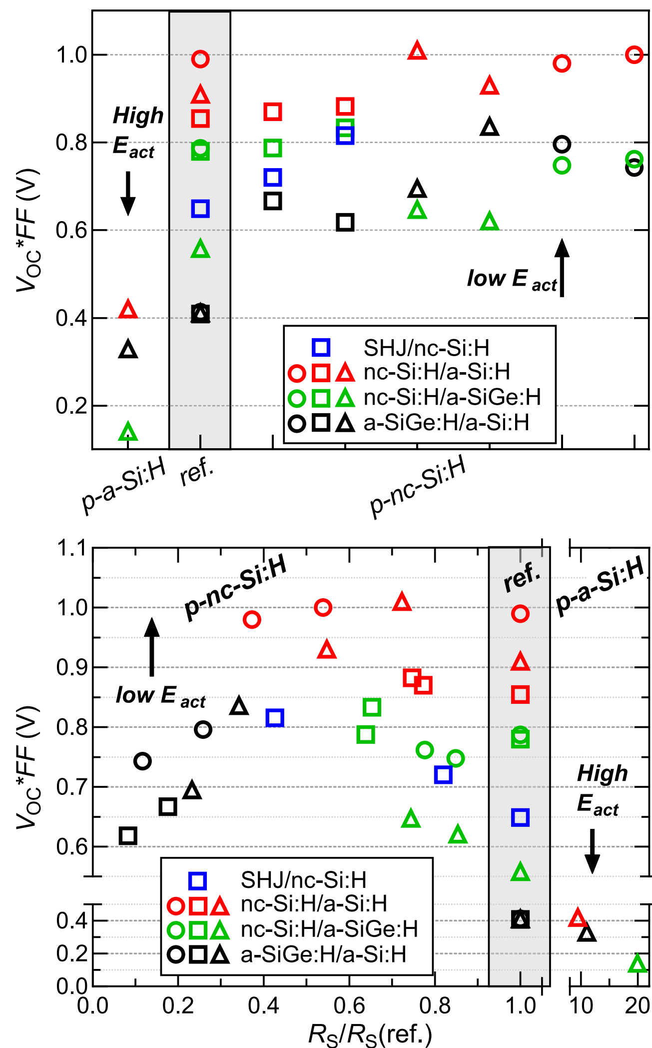

Fig. 6. The V_{oc}-FF product plotted as a function of the different contact layers (Top) and V_{oc}-FF product plotted as a function of change in series resistance (R_s) with respect to the reference sample without contact layer (bottom). Contact layers are processed on top of a 15–20 nm p-nc-SiO$_X$:H layer. Tick marks in top plot indicate samples with a 5 nm p-a-Si:H contact layer, no contact layer (ref) and 6 different low E_{act} 3–6 nm p-nc-Si:H contact layers, processed at different conditions (gas flow rates, power). The arrows and E_{act} designation indicate the E_{act} in reference to that of the single p-nc-SiO$_X$:H layer. The icons (triangle-square-circle) indicate series of samples processed at the same point in time with the exact same deposition conditions for all supporting layers. The colours indicates the multijunction architecture, namely SHJ/nc-Si:H (blue), nc-Si:H/a-Si:H (red), nc-Si:H/a-SiGe:H (green) and a-SiGe:H/a-Si:H (black).

impeded. For series **I**, for instance, the measured shunt resistance more than doubled by increasing the p-nc-SiO$_X$:H thickness from 5 nm to 10 nm, from ≈6300 Ω m^2 to ≈13600 Ω m^2. Further increasing the p-layer thickness results in increased recombination in the p-layer and at the i/p-interface, increasing the R_S and decreasing the FF.

Another important observation from the V_{oc} and FF of the devices is that the V_{oc}*FF product of the series with contact layer (series **III**) is significantly higher than that of the other two series. In fact, incorporating the contact layer results in a significant FF boost of about 9% absolute. This improvement is also apparent in Fig. 3, where the EQE's of series **III** are significantly higher than those of series **I**. Consequently, the next step is to investigate the influence of the contact layer properties.

3.4. Influence of the contact layer on the performance of tandem PV devices

To investigate the influence of the contact layer, the contact layer properties are varied, resulting in 7 different bi-layer configurations. A number of these bi-layer configuration variations were performed across four different tandem device architectures. The results are shown in Fig. 6(Top) where the V_{oc}*FF product is plotted for samples with a 5 nm p-type amorphous Si:H (p-a-Si:H) contact layer, no contact layer (ref) and 6 different 3–6 nm p-nc-Si:H contact layers that are processed at different conditions (gas flow rates, power) but all designed to have a low E_{act} compared to the p-nc-SiO$_X$:H layer. E_{act} determination is based on film measurements performed in earlier work [16,28].
The results clearly show that including a thin p-a-Si:H, which has a relatively high E_{act}, is detrimental to device performance. On the other hand, for nearly all series the V_{oc}*FF product is improved when a p-nc-Si:H contact layers is added. This indicates that the exact deposition conditions, and resulting material properties, of the thin contact layer are relatively unimportant. As long as they result in a low activation energy film, the contact layer will provide a performance boost in reference to a single p-nc-SiO$_X$:H layer.

Fig. 6(bottom) shows the relation between the series resistance (R_S) of the devices and the V_{oc}*FF product. By comparing the devices processed in a single series of experiments, so icons of similar type and colour, it can be observed that the V_{oc}*FF improvements are predominantly a results of the decreased R_S. A notable exception are the a-SiGe:H/a-Si:H tandem devices. For these devices, the addition of a contact layer leads to both a reduction of the R_S and an increase of the V_{oc}*FF product. Unlike the other tandems however, the devices with the contact layer resulting in the lowest R_S do not have the highest V_{oc}*FF product. This is because for these tandems, which have two thin amorphous absorbers, the shunt resistance had a dominant influence on the FF.

The results provide some clues as to the dominant loss mechanism in the devices. The recombination efficiency at the p/n-interface does not seem to be a limiting factor. More specifically, the availability of defects, or traps, at the p/n-interface to facilitate tunnelling is likely not limiting. In this case, trap-assisted tunnelling would potentially be improved by the addition of a thin defect-rich p-a-Si:H layer. Rather, the availability of holes at the p/n-interface, or the hole transport towards the p/n-interface is likely limiting. Fig. 7 shows how a low-E_{act} contact layer potentially improves hole availability. In the figure several band diagrams are schematically shown of the TRJ, visualizing the situation without contact layer (blue curve), with contact layer (red curve) and with a very low E_{act} contact layer (black curve). It can be observed that with decreasing E_{act}, the band bending changes such that the hole barrier is continuously decreased. Moreover, a position is created indicated position **X** in Fig. 7, spatially close to the electron accumulation position **I**, where holes can accumulate. This means that the introduction of a low E_{act} contact layer not only reduces the overall hole barrier and increases the overall electron barrier. It also creates an additional “pathway”, where the holes overcome two small energetic barriers, from position **II** to position **X** and subsequently to position **I**, rather than one large barrier. Consequently, with decreasing contact layer E_{act}, recombination occurs more efficiently at the TRJ as carriers are more effectively “directed” towards the p/n-interface, reducing the probability of recombination between generation and “desired” recombination at the p/n-interface.

3.5. Do we need p-nc-SiO$_X$:H?

The preceding section shows that devices with a p-nc-SiO$_X$:H/p-nc-Si:H bi-layer configuration have a much higher V_{oc}*FF product than devices without p-nc-Si:H layer. This begs the question: is the p-nc-SiO$_X$:H layer a requirement? In other words, would not a single 15–20 nm p-nc-Si:H layer outperform the bi-layer configurations?

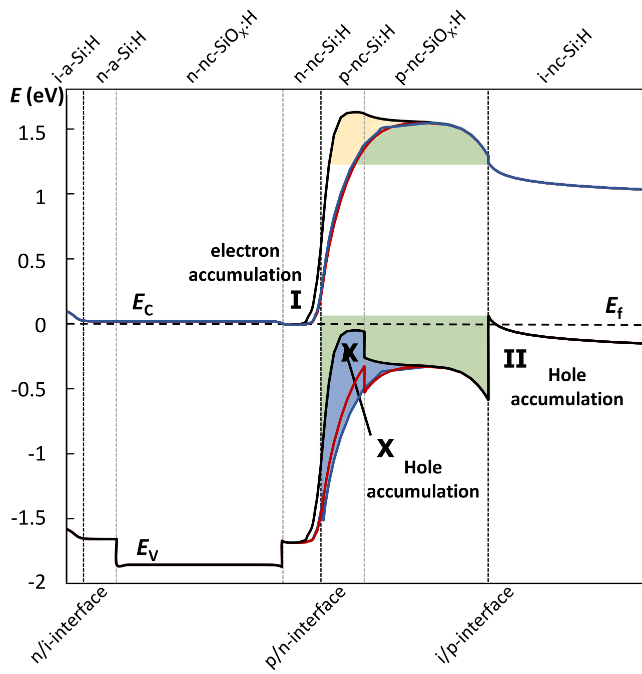

Fig. 7. Electrical simulations of the TRJ under equilibrium conditions in the dark. The energy band diagrams are shown for a single p-nc-SiO$_X$:H layer (blue), and two bi-layer configuration with a p-nc-Si:H contact layer with a low E_{act} of 250meV (red) and still lower E_{act} of 32meV (black). All p-layer stacks have a total thickness of 20 nm, the contact layers have thickness of 5 nm. For all configurations the conduction band edge E_C and valence band edge E_V are shown. The energy levels of the band edges are indicated in reference to the Fermi energy level E_f, positioned at 0 eV. The materials presented in the plots are indicated on top of the band diagram. The n/i-, p/n- and i/p-interfaces are indicated below the band diagram. The electron accumulation site at position **I**, and hole accumulation sites at positions **II** and **X** are referenced in the text. The coloured areas indicate the energy barriers for holes (bottom) and electrons (top), respectively. Blue areas indicate the barrier for a single p-nc-SiO$_X$:H layer, while the yellow areas indicates the barriers for the bi-layer configuration with the lowest E_{act} contact layer. The green area indicates an overlap between the two barriers.

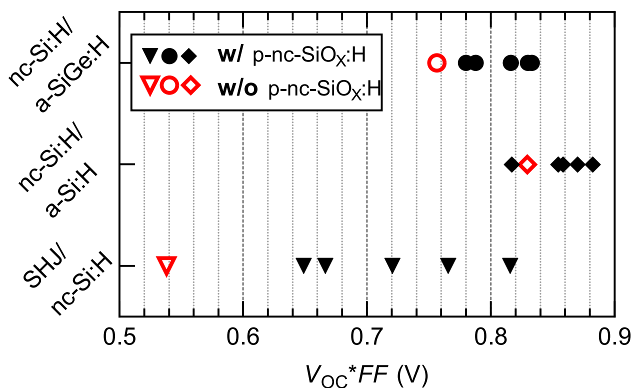

Fig. 8. V_{oc}-FF product for 3 different tandem device architectures. Red icons indicate a single p-nc-Si:H layer in the TRJ. Black icons indicate 5 different bi-layer p-nc-SiO$_X$:H/p-nc-SiO$_X$:H$^+$ and p-nc-SiO$_X$:H/p-nc-Si:H bi-layer configurations.

To answer this question, 6 different p-layer configurations are processed for 3 different tandem device architectures. The results are plotted in Fig. 8, where the red open icons represent the samples without p-nc-SiO$_X$:H layer. The other samples are different p-nc-SiO$_X$:H/p-nc-Si:H or p-nc-SiO$_X$:H/p-nc-SiO$_X$:H$^+$ bi-layer configurations. p-nc-SiO$_X$:H$^+$ indicates that the p-nc-SiO$_X$:H contact layer is processed with a higher F_{B2H6} flow rate in reference to the initial layer.

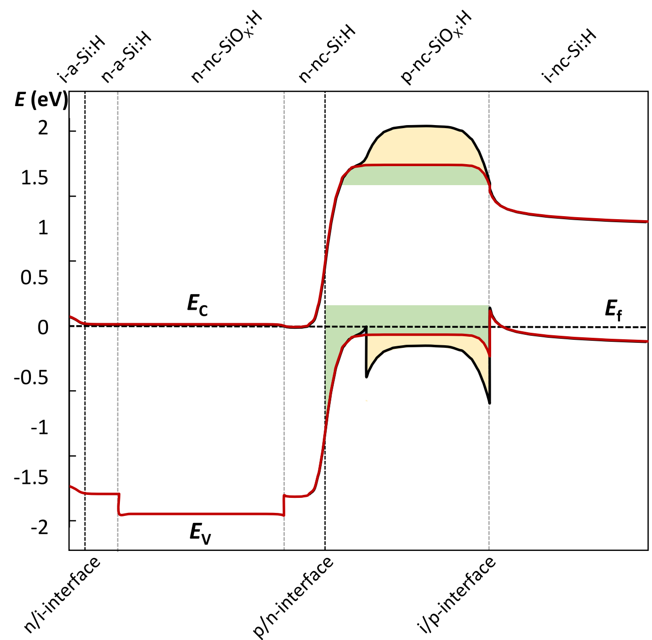

Fig. 9. Electrical simulations of the TRJ under equilibrium conditions in the dark. The energy band diagrams are shown for a 15 nm p-nc-SiO$_X$:H/ 5 nm p-nc-Si:H bilayer configuration (black) and a 20 nm p-nc-Si:H layer (red). For both p-layer stacks the E_C and valence band edge E_V are shown. The energy levels of the band edges are indicated in reference to the Fermi energy level E_f, positioned at 0 eV. The materials presented in the plots are indicated on top of the band diagram. The n/i-, p/n- and i/p-interfaces are indicated below the band diagram. The coloured areas indicate the energy barriers for holes (bottom) and electrons (top), respectively. The yellow area indicates the barrier for the bi-layer, while the blue areas indicates the barriers for the single p-nc-Si:H layer. The green area indicates an overlap between the two barriers.

It is apparent that the samples without p-nc-SiO$_X$:H layer are the worst in each series, with a single outlier, irrespective of device architecture. Clearly, the p-nc-SiO$_X$:H layer is a requirement for optimal tandem device performance. This is likely due to its high bandgap nature. The combination of high bandgap energy and low activation for a well performing p-contact has previously been reported for SHJ devices, where the p-contact is in contact with an n-type TCO [42]. The band diagrams in Fig. 9 show how the bi-layer configuration with p-nc-SiO$_X$:H can potentially improve performance with respect to a single p-nc-Si:H layer. Indicated in the visual is the situation where the E_G of the p-nc-SiO$_X$:H layer increases more strongly, with respect to the p-nc-Si:H layer, than the E_{act}. In this case, the electron barrier with respect to the hole barrier is increased. In both cases the p-nc-Si:H ensures good alignment at the p/n-interface. Alternatively, the high bandgap nature of the p-nc-SiO$_X$:H at the i/p-interface, or more specifically the larger difference between the conduction band edge and Fermi level in the p-layer, could decrease E_{Fp} and result in higher V_{bi} according to Eq. (2). This is especially true for higher bandgap absorbers. Finally, it should also be noted that better passivation by the predominantly amorphous p-nc-SiO$_X$:H at the i/p-interface, with respect to p-nc-Si:H, could also potentially positively affect the $V_{oc}*FF$ product of the tandem devices.

3.6. p-nc-SiO$_X$:H$^+$ contact layer doping

So far, the highest $V_{oc}*FF$ products have been achieved with a p-nc-SiO$_X$:H/p-nc-Si:H bi-layer configuration. The question is however, if the relatively low E_{act} of the p-nc-Si:H is indeed the reason behind the improved electrical performance of the tandem devices, could a similar improvement be achieved by a p-nc-SiO$_X$:H/p-nc-SiO$_X$:H$^+$ bi-layer configuration, where the p-nc-Si:H contact layer is replaced by a

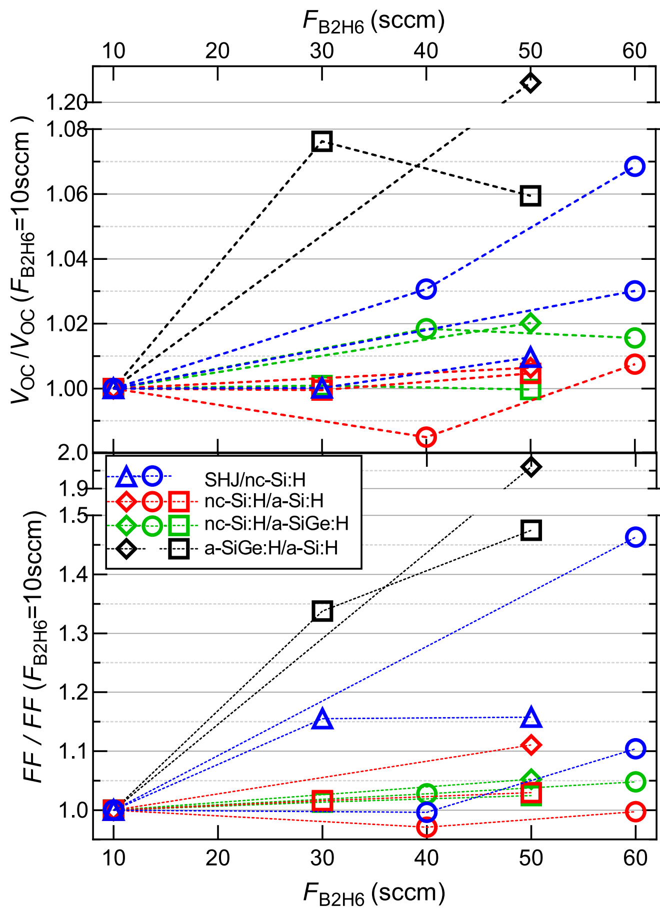

Fig. 10. V_{oc} (top) and FF (bottom) improvement in bi-layer p-nc-SiO$_X$:H/p-nc-SiO$_X$:H$^+$ configurations. Improvement is determined with respect to a reference sample processed without 3–5 nm p-nc-SiO$_X$:H$^+$ contact layer but of similar thickness. V_{oc} and FF improvements are plotted as a function of the diborane flow rate of the contact layer. The icons indicate series of samples processed at the same point in time with the exact same deposition conditions for all supporting layers. The colours indicates the multijunction architectures, namely SHJ/nc-Si:H (blue), nc-Si:H/a-Si:H (red), nc-Si:H/a-SiGe:H (green) and a-SiGe:H/a-Si:H (black).

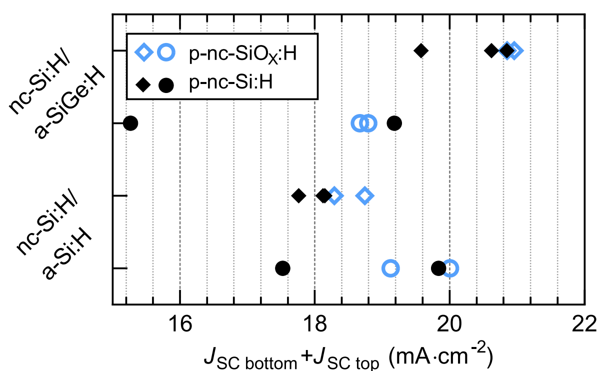

Fig. 11. The sum of the J_{sc} of the bottom junction and the J_{sc} of the top junction for two different series of nc-Si:H/a-Si:H (circles) and nc-Si:H/a-SiGe:H (diamonds) device architectures. J_{sc} for each junction is determined by weighing the measured spectral EQE curve with the AM1.5 g spectrum. All samples have a p-nc-SiO$_X$:H/p-Si:H bi-layer configuration, with p-nc-SiO$_X$:H (Blue, open symbols) and p-nc-Si:H (black, closed symbols) contact layers. The individual J_{sc}'s of the bottom and top junctions can be found in the supplementary information..

heavily doped p-nc-SiO$_X$:H layer? Such an alternative bi-layer configuration could potentially yield higher current densities because of the higher optical transparency of the p-nc-SiO$_X$:H layer.

Fig. 10 shows the relative improvement in FF (bottom) and V_{oc} (top) with respect to a single p-nc-SiO$_X$:H layer, as a function of F_{B2H6} of the p-nc-SiO$_X$:H$^+$ contact layer. The icons represent different series of cells. With a single outlier, strong improvements in performance with addition of a p-nc-SiO$_X$:H$^+$ layer can be observed, regardless of device architecture. For some samples, such as the nc-Si:H/a-SiGe:H tandems between 40–60 sccm and the a-SiGe:H/a-Si:H tandem between 30–50 sccm, the $V_{oc}*FF$ product improvement saturates, at which point there is a trade-off between V_{oc} and FF. For most series though the optimal F_{B2H6} is apparently located outside of the observed experimental range. The highest $V_{oc}*FF$ product of the devices with a p-nc-SiO$_X$:H/p-nc-SiO$_X$:H$^+$ bi-layer is comparable to that of the devices with a p-nc-SiO$_X$:H/p-nc-Si:H bi-layer. This would seem to indicate that the low E_{act} is the most important criteria for the contact layer in a bi-layer configuration. It should be noted that in Fig. 2, where the p-nc-SiO$_X$:H layer was not used in a bi-layer configuration, a significant decrease was observed in terms of $V_{oc}*FF$ product for F_{B2H6} ≥15–20 sccm. This is likely a result of "side effects" of increasing the dopant gas flow rate to p-nc-SiO$_X$:H material growth. These effects include a more porous amorphous growth with lower crystallinity and a larger a-SiO$_X$ material phase fraction [16]. The results show however that for a 3–6 nm contact layer these side-effects are minimal.

Since both bi-layer p-nc-SiO$_X$:H/p-nc-SiO$_X$:H$^+$ and p-nc-SiO$_X$:H/p-nc-Si:H bi-layer configurations yield similar $V_{oc}*FF$ products, the final question that remains is which bi-layer configuration should be used for optimal device performance. To answer this question, we consider the sum of the measured J_{sc}'s in the top and bottom junction of the tandem devices, as presented in Fig. 11. The figure shows the sum of the current densities for two different experimental series of bi-layer configurations, indicated by the circles and diamonds, applied in two different device architectures. It can be observed that the p-nc-SiO$_X$:H/p-nc-SiO$_X$:H$^+$ bi-layer configurations overall result in higher current densities, likely resulting from less parasitic absorption. Ultimately though, the choice for a specific bi-layer configuration will depend on the intended device architecture. Indeed, parasitic absorption in a 3–6 nm p-nc-Si:H layer positioned behind a 2000–3000 nm i-nc-Si:H absorber, in reference to the incident light, will be negligible. Consequently, the obtained $V_{oc}*FF$ products could be considered to indicate a level of freedom of design for p-nc-SiO$_X$:H/low-E_{act} bi-layer configurations in which the transmission and reflection at the TRJ's can be taken into account.

4. Conclusion

In this work the experimental results of a large number of SHJ/nc-Si:H, nc-Si:H/a-Si:H, nc-Si:H/a-SiGe:H and a-SiGe:H/a-Si:H multijunction devices are presented. The fundamental mechanisms behind the observed phenomena are qualitatively demonstrated using energy band diagrams obtained through electrical simulations in TCAD Sentaurus. The influence of thickness and design of the p-layer in the TRJ of these tandems are observed across different device architectures. It was found that for optimal device performance in terms of $V_{oc}*FF$ product, the presence of a high bandgap p-nc-SiO$_X$:H layer is crucial, and the optimal thickness is in the range of 12–18 nm. Moreover, a strong improvement was observed when a thin, low activation energy contact layer was used in combination with the p-nc-SiO$_X$:H layer. High $V_{oc}*FF$ products could be achieved both by p-nc-SiO$_X$:H/ p-nc-SiO$_X$:H$^+$ and p-nc-SiO$_X$:H/p-nc-Si:H bi-layer configurations.

Declaration of competing interest

The authors declare that they have no known competing financial interests or personal relationships that could have appeared to influence the work reported in this paper.

Acknowledgements

The authors would like to gratefully acknowledge the financial support from the Netherlands Organization for Scientific Research (NWO) Solar to Products grant and the support provided by Shell International Exploration & Production New Energies Research & Technology Dense Energy Carriers Program.

Appendix A. Supplementary data

Supplementary material related to this article can be found online at https://doi.org/10.1016/j.solmat.2021.111501.

References

[1] J. Lehr, M. Langenhorst, R. Schmager, F. Gota, S. Kirner, U. Lemmer, B.S. Richards, C. Case, U.W. Paetzold, Energy yield of bifacial textured perovskite/silicon tandem photovoltaic modules, Sol. Energy Mater. Sol. Cells 208 (December 2019) (2020) 110367, http://dx.doi.org/10.1016/j.solmat.2019.110367.

[2] M. Jaysankar, S. Paetel, E. Ahlswede, U.W. Paetzold, T. Aernouts, R. Gehlhaar, J. Poortmans, Toward scalable perovskite-based multijunction solar modules, Prog. Photovolt., Res. Appl. (2019) pip.3153, http://dx.doi.org/10.1002/pip.3153.

[3] J. Li, L. Jiang, M. Chen, X. Li, Y. Wei, Y. Ma, Z. Fu, Y. Yan, Structure and physical properties evolution of ITO film during amorphous-crystalline transition using a highly effective annealing technique, Ceram. Int. 45 (13) (2019) 16214–16225, http://dx.doi.org/10.1016/j.ceramint.2019.05.143.

[4] A. Hajijafarassar, F. Martinho, F. Stulen, S. Grini, S. López-Mariño, M. Espíndola-Rodríguez, M. Döbeli, S. Canulescu, E. Stamate, M. Gansukh, S. Engberg, A. Crovetto, L. Vines, J. Schou, O. Hansen, Monolithic thin-film chalcogenide–silicon tandem solar cells enabled by a diffusion barrier, Sol. Energy Mater. Sol. Cells 207 (December 2019) (2020) 110334, http://dx.doi.org/10.1016/j.solmat.2019.110334.

[5] R. Cariou, J. Benick, F. Feldmann, O. Höhn, H. Hauser, P. Beutel, N. Razek, M. Wimplinger, B. Bläsi, D. Lackner, M. Hermle, G. Siefer, S.W. Glunz, A.W. Bett, F. Dimroth, III–V-On-silicon solar cells reaching 33% photoconversion efficiency in two-terminal configuration, Nat. Energy 3 (4) (2018) 326–333, http://dx.doi.org/10.1038/s41560-018-0125-0.

[6] S. Fan, Z.J. Yu, Y. Sun, W. Weigand, P. Dhingra, M. Kim, R.D. Hool, E.D. Ratta, Z.C. Holman, M.L. Lee, 20%-efficient epitaxial GaAsP/Si tandem solar cells, Sol. Energy Mater. Sol. Cells 202 (March) (2019) 110144, http://dx.doi.org/10.1016/j.solmat.2019.110144.

[7] P. Perez-Rodriguez, W. Vijselaar, J. Huskens, M. Stam, M. Falkenberg, M. Zeman, W. Smith, A.H. Smets, Designing a hybrid thin-film/wafer silicon triple photovoltaic junction for solar water splitting, Prog. Photovolt., Res. Appl. 27 (3) (2019) 245–254, http://dx.doi.org/10.1002/pip.3085.

[8] S. Kirner, H. Sarajan, A. Azarpira, T. Schedel-Niedrig, B. Stannowski, B. Rech, R. Schlatmann, Wafer surface tuning for a-Si:H/μc-Si:H/c-Si triple junction solar cells for application in water splitting, Energy Procedia 102 (2016) 126–135, http://dx.doi.org/10.1016/j.egypro.2016.11.327.

[9] P. Buehlmann, J. Bailat, D. Dominé, A. Billet, F. Meillaud, A. Feltrin, C. Ballif, In situ silicon oxide based intermediate reflector for thin-film silicon micromorph solar cells, Appl. Phys. Lett. 91 (14) (2007) 143505, http://dx.doi.org/10.1063/1.2794423.

[10] L.V. Mercaldo, P. Delli Veneri, I. Usatii, E.M. Esposito, G. Nicotra, Properties of mixed phase n-doped silicon oxide layers and application in micromorph solar cells, Sol. Energy Mater. Sol. Cells 119 (2013) 67–72, http://dx.doi.org/10.1016/j.solmat.2013.05.030.

[11] J. Cashmore, M. Apolloni, A. Braga, O. Caglar, V. Cervetto, Y. Fenner, S. Goldbach-Aschemann, C. Goury, J. Hötzel, T. Iwahashi, J. Kalas, M. Kitamura, M. Klindworth, M. Kupich, G.-F. Leu, J. Lin, M.-H. Lindic, P. Losio, T. Mates, D. Matsunaga, B. Mereu, X.-V. Nguyen, I. Psimoulis, S. Ristau, T. Roschek, A. Salabas, E. Salabas, I. Sinicco, Improved conversion efficiencies of thin-film silicon tandem (MICROMORPH™) photovoltaic modules, Sol. Energy Mater. Sol. Cells 144 (2016) 84–95, http://dx.doi.org/10.1016/j.solmat.2015.08.022.

[12] F. Hou, C. Han, O. Isabella, L. Yan, B. Shi, J. Chen, S. An, Z. Zhou, W. Huang, H. Ren, Q. Huang, G. Hou, X. Chen, Y. Li, Y. Ding, G. Wang, C. Wei, D. Zhang, M. Zeman, Y. Zhao, X. Zhang, Inverted pyramidally-textured PDMS antireflective foils for perovskite/silicon tandem solar cells with flat top cell, Nano Energy 56 (October 2018) (2019) 234–240, http://dx.doi.org/10.1016/j.nanoen.2018.11.018.

[13] M. Boccard, M. Despeisse, J. Escarre, X. Niquille, G. Bugnon, S. Hanni, M. Bonnet-Eymard, F. Meillaud, C. Ballif, High-stable-efficiency tandem thin-film silicon solar cell with low-refractive-index silicon-oxide interlayer, IEEE J. Photovolt. 4 (6) (2014) 1368–1373, http://dx.doi.org/10.1109/JPHOTOV.2014.2357495.

[14] S. Kirner, M. Hammerschmidt, C. Schwanke, D. Lockau, S. Calnan, T. Frijnts, S. Neubert, A. Schopke, F. Schmidt, J.-H. Zollondz, A. Heidelberg, B. Stannowski, B. Rech, R. Schlatmann, Implications of TCO topography on intermediate reflector design for a-Si/μc-Si tandem solar cells—Experiments and rigorous optical simulations, IEEE J. Photovolt. 4 (1) (2014) 10–15, http://dx.doi.org/10.1109/JPHOTOV.2013.2279204.

[15] S.-j. Jung, B.-j. Kim, M. Shin, Low-refractive-index and high-transmittance silicon oxide with a mixed phase of n-type microcrystalline silicon as intermediate reflector layers for tandem solar cells, Sol. Energy Mater. Sol. Cells 121 (2014) 1–7, http://dx.doi.org/10.1016/j.solmat.2013.10.036, URL https://linkinghub.elsevier.com/retrieve/pii/S0927024813005576.

[16] T. de Vrijer, A.H. Smets, The relation between precursor gas flows, thickness dependent material phases and opto-electrical properties of doped a/nc-SiO$_{X\geq0}$:H films, IEEE J. Photovolt. (2021) 1–9, http://dx.doi.org/10.1109/JPHOTOV.2021.3059940.

[17] Y. Zhao, L. Mazzarella, P. Procel, C. Han, G. Yang, A. Weeber, M. Zeman, O. Isabella, Doped hydrogenated nanocrystalline silicon oxide layers for high-efficiency c-Si heterojunction solar cells, Prog. Photovolt., Res. Appl. 28 (5) (2020) 425–435, http://dx.doi.org/10.1002/pip.3256.

[18] G. Yang, R.A. van Swaaij, H. Tan, O. Isabella, M. Zeman, Modulated surface textured glass as substrate for high efficiency microcrystalline silicon solar cells, Sol. Energy Mater. Sol. Cells 133 (2015) 156–162, http://dx.doi.org/10.1016/j.solmat.2014.11.013.

[19] H. Tan, E. Psomadaki, O. Isabella, M. Fischer, P. Babal, R. Vasudevan, M. Zeman, A.H.M. Smets, Micro-textures for efficient light trapping and improved electrical performance in thin-film nanocrystalline silicon solar cells, Appl. Phys. Lett. 103 (17) (2013) 173905, http://dx.doi.org/10.1063/1.4826639.

[20] T. de Vrijer, H. Parasramka, S.J. Roerink, A.H.M. Smets, An expedient semi-empirical modelling approach for optimal bandgap profiling of stoichiometric absorbers: A case study of thin film amorphous silicon germanium for use in multijunction photovoltaic devices, Sol. Energy Mater. Sol. Cells 225 (March) (2021) 111051, http://dx.doi.org/10.1016/j.solmat.2021.111051.

[21] T. de Vrijer, A.H.M. Smets, Advanced textured monocrystalline silicon substrates with high optical scattering yields and low electrical recombination losses for supporting crack-free nano- to poly-crystalline film growth, Energy Sci. Eng. (November 2020) (2021) http://dx.doi.org/10.1002/ese3.873.

[22] Synopsys, Sentaurus TCAD Datasheet, Tech. Rep., 2018.

[23] P. Procel, H. Xu, A. Saez, C. Ruiz-Tobon, L. Mazzarella, Y. Zhao, C. Han, G. Yang, M. Zeman, O. Isabella, The role of heterointerfaces and subgap energy states on transport mechanisms in silicon heterojunction solar cells, Prog. Photovolt., Res. Appl. 28 (9) (2020) 935–945, http://dx.doi.org/10.1002/pip.3300.

[24] S. Schicho, Amorphous and Microcrystalline Silicon Applied in Very Thin Tandem Solar Cells, Forschungszentrum Jülich, 2011.

[25] P. Procel, G. Yang, O. Isabella, M. Zeman, Theoretical evaluation of contact stack for high efficiency IBC-SHJ solar cells, Sol. Energy Mater. Sol. Cells 186 (May) (2018) 66–77, http://dx.doi.org/10.1016/j.solmat.2018.06.021.

[26] M. Boccard, P. Cuony, M. Despeisse, D. Dominé, A. Feltrin, N. Wyrsch, C. Ballif, Substrate dependent stability and interplay between optical and electrical properties in μc-Si:H single junction solar cells, Sol. Energy Mater. Sol. Cells 95 (1) (2011) 195–198, http://dx.doi.org/10.1016/j.solmat.2010.04.043.

[27] V. Smirnov, A. Lambertz, B. Grootoonk, R. Carius, F. Finger, Microcrystalline silicon oxide (μc-Siox:H) alloys: A versatile material for application in thin film silicon single and tandem junction solar cells, J. Non-Cryst. Solids 358 (17) (2012) 1954–1957, http://dx.doi.org/10.1016/j.jnoncrysol.2011.12.019.

[28] T. de Vrijer, F.T. Si, H. Tan, A.H. Smets, Chemical stability and performance of doped silicon oxide layers for use in thin film silicon solar cells, IEEE J. Photovolt. 9 (1) (2019) 3–11, http://dx.doi.org/10.1109/PVSC.2018.8548192.

[29] M. Bonnet-Eymard, M. Boccard, G. Bugnon, F. Meillaud, M. Despeisse, F.-J. Haug, C. Ballif, Current matching optimization in high-efficiency thin-film silicon tandem solar cells, in: 2013 IEEE 39th Photovoltaic Specialists Conference, PVSC, IEEE, 2013, pp. 0184–0187, http://dx.doi.org/10.1109/PVSC.2013.6744126.

[30] B. Yan, G. Yue, J. Yang, S. Guha, Correlation of current mismatch and fill factor in amorphous and nanocrystalline silicon based high efficiency multi-junction solar cells, in: 33rd IEEE Photovolatic Specialists Conference, IEEE, 2008, pp. 1–6, http://dx.doi.org/10.1109/PVSC.2008.4922607.

[31] V. Smirnov, A. Lambertz, S. Moll, M. Bär, D.E. Starr, R.G. Wilks, M. Gorgoi, A. Heidt, M. Luysberg, B. Holländer, F. Finger, Doped microcrystalline silicon oxide alloys for silicon-based photovoltaics: Optoelectronic properties, chemical composition, and structure studied by advanced characterization techniques, Phys. Status Solidi (A) 213 (7) (2016) 1814–1820, http://dx.doi.org/10.1002/pssa.201533022.

[32] P. Cuony, D.T.L. Alexander, I. Perez-Wurfl, M. Despeisse, G. Bugnon, M. Boccard, T. Söderström, A. Hessler-Wyser, C. Hébert, C. Ballif, Silicon filaments in silicon oxide for next-generation photovoltaics, Adv. Mater. 24 (9) (2012) 1182–1186, http://dx.doi.org/10.1002/adma.201104578.

[33] M. Klingsporn, S. Kirner, C. Villringer, D. Abou-Ras, I. Costina, M. Lehmann, B. Stannowski, Resolving the nanostructure of plasma-enhanced chemical vapor deposited nanocrystalline SiOx layers for application in solar cells, J. Appl. Phys. 119 (22) (2016) 223104, http://dx.doi.org/10.1063/1.4953566.

[34] C. Song, X. Wang, R. Huang, J. Song, Y. Guo, Effects of doping concentration on the microstructural and optoelectrical properties of boron doped amorphous and nanocrystalline silicon films, Mater. Chem. Phys. 142 (1) (2013) 292–296, http://dx.doi.org/10.1016/j.matchemphys.2013.07.017.

[35] A. Richter, L. Zhao, F. Finger, K. Ding, Nano-composite microstructure model for the classification of hydrogenated nanocrystalline silicon oxide thin films, Surf. Coat. Technol. 295 (2016) 119–124, http://dx.doi.org/10.1016/j.surfcoat.2015.09.016.

[36] D.B. Saint John, H.-B. Shin, M.-Y. Lee, S.K. Ajmera, A.J. Syllaios, E.C. Dickey, T.N. Jackson, N.J. Podraza, Influence of microstructure and composition on hydrogenated silicon thin film properties for uncooled microbolometer applications, J. Appl. Phys. 110 (3) (2011) 033714, http://dx.doi.org/10.1063/1.3610422.

[37] H. Fujiwara, M. Kondo, A. Matsuda, Real-time studies of amorphous and microcrystalline Si:H growth by spectroscopic ellipsometry and infrared spectroscopy, Thin Solid Films 455–456 (2004) 670–674, http://dx.doi.org/10.1016/j.tsf.2003.11.233.

[38] A. Lambertz, T. Grundler, F. Finger, Hydrogenated amorphous silicon oxide containing a microcrystalline silicon phase and usage as an intermediate reflector in thin-film silicon solar cells, J. Appl. Phys. 109 (11) (2011) 113109, http://dx.doi.org/10.1063/1.3592208.

[39] S. Kirner, S. Calnan, O. Gabriel, S. Neubert, M. Zelt, B. Stannowski, B. Rech, R. Schlatmann, An improved silicon-oxide-based intermediate-reflector for micromorph solar cells, Phys. Status Solidi (C) 9 (10–11) (2012) 2145–2148, http://dx.doi.org/10.1002/pssc.201200243.

[40] P.-W. Chen, P.-L. Chen, C.-C. Tsai, Development of wider bandgap n-type a-Siox:H and μc-SiOx:H as both doped and intermediate reflecting layer for a-Si:H/a-$Si_{1-X}Ge_X$:H tandem solar cells, Electron. Mater. Lett. 12 (4) (2016) 445–450, http://dx.doi.org/10.1007/s13391-016-4004-1.

[41] M. Vukadinović, F. Smole, M. Topič, R.E.I. Schropp, F.A. Rubinelli, Transport in tunneling recombination junctions: A combined computer simulation study, J. Appl. Phys. 96 (12) (2004) 7289–7299, http://dx.doi.org/10.1063/1.1811375.

[42] Y. Zhao, P. Procel, C. Han, L. Mazzarella, G. Yang, A. Weeber, M. Zeman, O. Isabella, Design and optimization of hole collectors based on nc-SiO_x :H for high-efficiency silicon heterojunction solar cells, Sol. Energy Mater. Sol. Cells 219 (2021) 110779, http://dx.doi.org/10.1016/j.solmat.2020.110779.